



Evolution of Thermally Driven Disk Wind in the Black Hole Binary 4U 1630–47 Observed with *Suzaku* and *NuSTAR*

Takafumi Hori¹ , Yoshihiro Ueda¹ , Chris Done², Megumi Shidatsu³, and Aya Kubota⁴

¹ Department of Astronomy, Kyoto University, Kitashirakawa-Oiwake-cho, Sakyo-ku, Kyoto 606-8502, Japan; ueda@kustastro.kyoto-u.ac.jp

² Department of Physics, University of Durham, South Road, Durham, DH1 3LE, UK

³ Department of Physics, Ehime University, Matsuyama 790-8577, Japan

⁴ Department of Electronic Information Systems, Shibaura Institute of Technology, 307 Fukasaku, Minuma-ku, Saitama 337-8570, Japan

Received 2018 January 11; revised 2018 October 16; accepted 2018 October 20; published 2018 December 26

Abstract

We performed simultaneous observations with *Suzaku* and *NuSTAR* of the Galactic black hole binary 4U 1630–47 in the high/soft state (HSS) during the 2015 outburst. To compare our results with those observed in the HSS at lower luminosities, we reanalyze the *Suzaku* data taken during the 2006 outburst. The continuum can be well explained by thermal disk emission and a hard power-law tail. All spectra show strong iron-K absorption line features, suggesting that a disk wind is always developed in the HSS. We find that the degree of ionization of the wind dramatically increased at the brightest epoch in 2015, when the continuum became harder. Detailed XSTAR simulations show that this cannot be explained solely by an increase of the photoionization flux. Instead, we show that the observed behavior in the HSS is consistent with a theory of thermally driven disk winds, where the column density and the ionization parameter of the disk wind are proportional to the luminosity and the Compton temperature, respectively.

Key words: accretion, accretion disks – black hole physics – stars: individual (4U 1630–47) – X-rays: binaries

1. Introduction

Modern X-ray spectroscopy has revealed that highly ionized disk winds are a ubiquitous feature in accreting black hole binaries (BHBs). Disk winds intercept X-ray photons emitted from the central source and produce absorption lines from highly ionized ions in the observed spectra (e.g., Ueda et al. 1998; Kotani et al. 2000; Miller et al. 2006b; Kubota et al. 2007; Ueda et al. 2009; Díaz Trigo et al. 2012). Since these absorption lines are mainly observed in high inclination angle systems, it is thought that these winds are aligned along the disk plane with an opening angle of a few tens of degrees (Ponti et al. 2012). While disk winds seem to always be present in the high/soft state (HSS), the absorption line features disappear in the low/hard state (Ponti et al. 2012) with a few exceptions (Shidatsu et al. 2013). Understanding of the nature of disk winds is indispensable to build the whole picture of accretion disk dynamics in BHBs since a huge amount of accreted matter is carried away by them (e.g., Kotani et al. 2000; Miller et al. 2006a; Ueda et al. 2009; Neilsen et al. 2011).

Three major theoretical models have been proposed as the origin of the disk wind in X-ray binaries; radiatively driven, thermally driven, and magnetically driven winds (see, e.g., Done et al. 2007). Radiatively driven winds can be produced when the radiation pressure is sufficiently large. As the source luminosity L approaches the Eddington limit L_{edd} , the “effective” gravity decreases by a factor of $1 - L/L_{\text{edd}}$; Ueda et al. (2004) showed that a wind can be launched when a gas in Keplerian motion is exposed to the radiation with $L > 0.5L_{\text{edd}}$. Thermally driven winds can be launched at even lower luminosities. When X-rays from the central source heat up an upper layer of the accretion disk to the Compton temperature T_{IC} that is higher than the gravitational binding potential at that radius, the gas will be released from the system by its thermal pressure (Begelman et al. 1983). Here, T_{IC} is calculated from the X-ray spectra by considering the equilibrium of

Compton-heating and Compton-cooling photons:

$$T_{\text{IC}} = \frac{1}{4k_{\text{B}}} \frac{\int_0^{\infty} h\nu L_{\nu} d\nu}{\int_0^{\infty} L_{\nu} d\nu}. \quad (1)$$

Finally, magnetically driven winds may be formed by magnetohydrodynamics effects, where magnetic field transports the angular momentum from the disk outward (Penna et al. 2010).

It is not clear whether or not all disk winds in BHBs have a common, unique origin. Previous studies suggested that most disk winds are consistent with thermally driven ones on the basis of their estimated locations (e.g., Kubota et al. 2007). By contrast, evidence for a magnetically driven wind was reported in GRO J1655–40 by Miller et al. (2006a), who found that the launching radius is much smaller than that expected from a thermally driven wind by using a diagnostic of the density sensitive lines. Uttley & Klein-Wolt (2015) demonstrated that this high-density wind appeared during a nonstandard accretion and variability state. The interpretation of this particular case is still under debate, however (e.g., Netzer 2006; Miller et al. 2008; Kallman et al. 2009; Neilsen et al. 2016; Shidatsu et al. 2016; Done et al. 2018). For instance, recent works suggest that the wind may be Compton-thick, shielding substantial intrinsic X-ray emission, and that radiative pressure may play a critical role to drive this wind. From analyses of the multi-wavelength spectral energy distribution, Neilsen et al. (2016) and Shidatsu et al. (2016) estimated the intrinsic luminosity to be several tens of times and $\gtrsim 0.7$ times the Eddington luminosity, assuming that the optical flux is dominated by the blackbody emission from the photosphere of the wind, and by the irradiated disk emission from the outer disk, respectively. Thus, it is very important to do more observational tests to identify the origin of disk winds.

4U 1630–47 is an ideal BHB to investigate the properties of the disk wind thanks to its brightness and frequent outbursts.

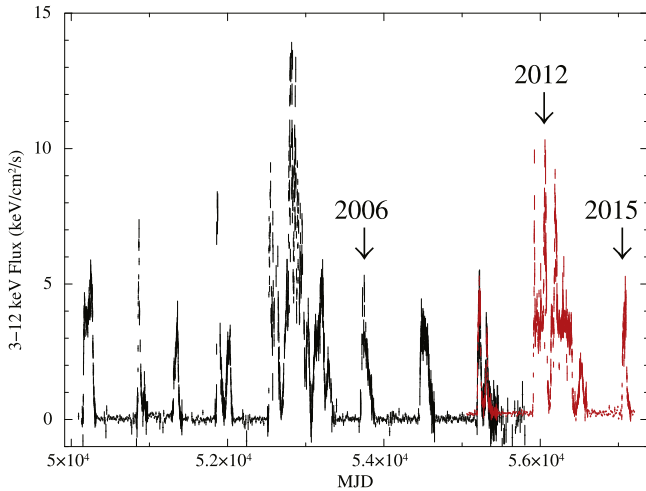


Figure 1. Long-term light curves of 4U 1630–47 in the 3–12 keV band obtained with *RXTE*/ASM (black) and *MAXI*/GSC (red). Two long outbursts occurred around MJD = 53,000 and MJD = 56,000. The 2006, 2012, and 2015 outbursts are indicated by the down arrows.

Figure 1 shows the overall light curve of 4U 1630–47 obtained with the All Sky Monitor (ASM) on board the Rossi X-ray Timing Explorer (*RXTE*; Levine et al. 1996) and with the Gas Slit Camera (GSC) on board the Monitor of All-sky X-ray Image (*MAXI*; Matsuoka et al. 2009). Here the count rates of the *RXTE*/ASM light curve are converted to the energy fluxes by using Equation (A1) in Zdziarski et al. (2002), and those of the *MAXI* light curve in the 4–10 keV band are converted to the 3–12 keV fluxes by assuming the Crab spectra. As noticed, 4U 1630–47 exhibits quasi-periodic outbursts with a 600–700 day cycle. Kubota et al. (2007) detected H-like and He-like iron absorption lines from six observations in the HSS with *Suzaku* during the 2006 outburst (indicated by the down arrow in Figure 1). They found that these absorption lines became weaker with increasing luminosity, which is consistent with a photoionization scenario. King et al. (2014) also reported the highly ionized absorption lines during the 2012 outburst when the source was in a very similar state to those observed by Kubota et al. (2007). Hori et al. (2014) observed 4U 1630–47 in the very high state (VHS) around the peak of the 2012 outburst with *Suzaku*, and found that the iron-K absorption lines disappeared in this state. The absence of these features in the VHS was also reported by Díaz Trigo et al. (2014) by using the *XMM-Newton* data.

In this paper, we present the results of simultaneous observations of 4U 1630–47 with *Suzaku* and *NuSTAR* on three occasions during the 2015 outburst. A part of the preliminary results were reported in Hori et al. (2016), which should be superseded by this work. Combining with the *Suzaku* results in the 2007 outburst, we examine the evolution of the iron-K absorption lines in the HSS. Section 2 describes the observation and data reduction. The results of the spectral analysis are presented in Section 3. We discuss the origin of the disk wind by comparison with a theoretical model in Section 4, and summarize our conclusions in Section 5. For convenience of discussion, we always assume the distance of $D = 10$ kpc and inclination angle of $i = 70^\circ$ as reference values, which are all unknown for this target. Solar abundances by Anders & Grevesse (1989) are adopted. The errors in spectral parameters are given at 90% confidence limits for a single parameter of interest unless otherwise stated.

2. Observation and Data Reduction

Figure 2 shows blow-ups of the X-ray light curves of 4U 1630–47 during the 2006 (a), 2012 (b), and 2015 (c) outbursts. The top, middle, and bottom panels plot those in the 3–12 keV band obtained with *RXTE*/ASM (a) or with *MAXI*/GSC (b and c, converted from the 4–10 keV count rate by assuming the Crab spectrum), those in the 15–50 keV band obtained with the Burst Alert Telescope (BAT) on board *Swift* (Burrows et al. 2005), and their hardness ratio (3–12 keV/15–50 keV), respectively. Three ToO (Target of Opportunity) observations of 4U 1630–47 were performed with *Suzaku* on 2015 February 20, 24, and 27, simultaneously with *NuSTAR* (Harrison et al. 2013) for the first two epochs. The overall behavior of the 2015 outburst was quite complex, showing several spiky peaks around the maximum luminosity. Our ToO observations, whose epochs are indicated by the dotted lines in Figure 2(c), were made around the second peak of the outburst. The luminosity in the 2–6 keV band was the highest in the first epoch among the three, and those in the second and third ones were similar to each other (Table 1).

Suzaku carried two types of detectors, the X-ray Imaging Spectrometer (XIS) and the Hard X-ray Detector (HXD). At the time of our observations, two front-side-illuminated XISs (FI-XISs) XIS0 and XIS3, and one back-side-illuminated XIS (BI-XIS), XIS1, were available, whereas the HXD was turned off due to the power shortage of the spacecraft. All XISs were operated with the one-fourth window mode and the 0.3 s burst option to avoid pileup effects. We utilized the “cleaned” event files reduced by the pipeline processing version 2.8.20.37 and analyzed them in a standard manner with HEASOFT version 6.16 and calibration database released on 2015 March 12. We estimated the fraction of piled-up events using the `aepi-leupcheckup.py` tool,⁵ and found that it could be reduced to <1% by excluding the central circular region with a radius of 0.3. Hence, the XIS spectra were integrated within an annular region with an inner and an outer radius of 0.3 and 1.3, respectively. Comparing with the spectra integrated with larger inner radii, we confirmed that the pileup effects were negligible in our spectra at energies up to 9 keV. The background spectra were taken from a circular region with a radius of 1.3 away from the source by 7'. Further details about these observations are listed in Table 1.

NuSTAR has two Focal Plane Modules (FPM), A and B. The *NuSTAR* data were reduced with the standard pipeline NUPIPELINE version 0.4.3 and were analyzed with NUSTARDAS software version 1.4.1 included in HEASOFT version 6.16. The source spectra were extracted from a central 100'' circular region around the target by using the standard tool NUPRODUCTS. We extracted the background spectra from an annular region with an inner and an outer radius of 240'' and 260'', respectively. The exposure times are listed in Table 1.

We found that the FI-XIS spectra were apparently harder than the BI-XIS spectra, most probably due to the cross-calibration error, as reported in recent *Suzaku* data (e.g., Shidatsu et al. 2013). Hence, these differences were approximately corrected by multiplying the FI-XIS spectra by a power-law function with a photon index of -0.10 in spectral fitting.

⁵ http://www-x.phys.se.tmu.ac.jp/~syamada/ana/suzaku/XISPileupDoc_20120221/XIS_PileupDoc_20120220_ver1.1.html

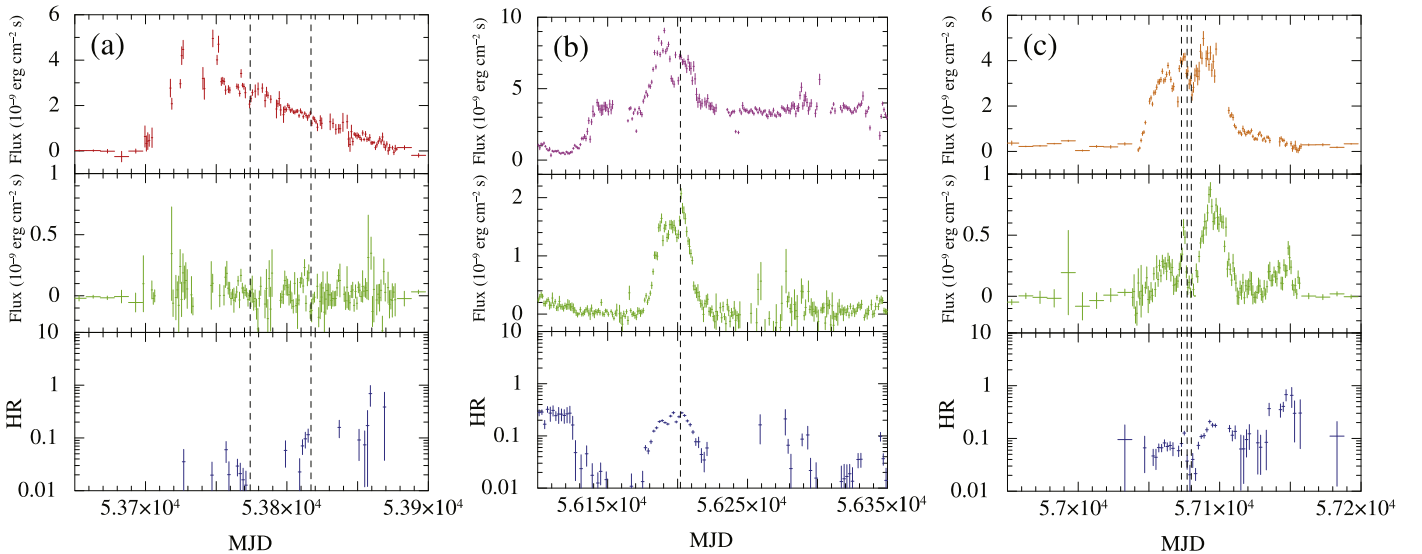


Figure 2. (Top) Expanded light curves of 4U 1630–47 in the 3–12 keV band during 2006 (a), 2012 (b), and 2015 (c) outburst, observed with *RXTE*/ASM for (a) and *MAXI*/GSC for (b) and (c). (Middle) Those in the 15–50 keV obtained with *Swift*/BAT. (Lower) The hardness ratio between the two bands. The dashed lines represent the epochs of the *Suzaku* observations.

This procedure made much better agreement of the FI spectra with the BI-XIS and *NuSTAR* spectra.

We reanalyzed the *Suzaku* archive data taken during the 2006 outburst (obsid = 400010010 through 400010060), which were analyzed and published by Kubota et al. (2007), to compare our results to those of previous *Suzaku* observations. The shape of the light curves (Figure 2(a)), characterized by a fast rise and a gradual decay, were less complex than that of the 2015 outburst. The right and left dashed lines in this figure represent the epochs of the first (obsid = 400010010) and the last (obsid = 400010060) observations, respectively. The details of these observations are also listed in Table 1. Because all observations in 2006 suffer from pileup effects, these spectra were extracted within an annular region with an inner and an outer radius of $1'$ and $1'.7$, respectively, so that the pileup fraction should be less than 1%.

Figure 3 shows the time-averaged spectra in the 2006 and 2015 outbursts. The overall spectral shapes are almost the same in these observations, except that in the brightest observation in the 2015 outburst (orange), which showed a stronger hard power-law tail. Hereafter, we refer to the first to sixth observations in 2006, the second observation in 2015, and the first one in 2015 as OBS 1 to 6, 7, and 8, respectively (in order of increasing luminosity). We refer to the third observation during the 2015 outburst as OBS 0 and treat it separately because no hard X-ray data above 10 keV are available. As an exception, the VHS observation in 2012 is referred to as OBS α . We note that the spectra in OBS 7 (blue) became slightly softer than that in OBS 6 (red). We note that the spectra of OBS 7 is very similar to the spectrum of OBS 6 taken 9 years before, except that the hard tail is slightly fainter.

For comparison, we also plot the VHS spectra (OBS α) observed in the 2012 outburst, which was published by Hori et al. (2014). The flux responsible for photoionization of iron ions (i.e., above ~ 9 keV) in this observation was much higher than in the HSS. The spectrum did not show any iron-K absorption line feature that are ubiquitously detected in the HSS (OBS 1–8). Hori et al. (2014) showed that iron ions in the disk wind could not have been fully ionized only by the

increase of photoionizing photons, if their physical parameters (location and density) had been the same as those in the HSS.

3. Spectral Analysis

3.1. Effect of Dust Scattering

Since 4U 1630–47 suffers from heavy absorption by the interstellar matter ($N_{\text{H}} \sim 8 \times 10^{22} \text{ cm}^{-2}$), effects by the dust scattering are not negligible (Smith et al. 2002; Ueda et al. 2010). A part of the direct emission is “scattered-out” by interstellar dust in the line of sight, while photons emitted with slightly different angles from the line of sight are “scattered-in” toward the observer, producing a dust-scattering halo around the source. When the source flux and spectrum is constant, integrating all scattered-in photons will cancel the scattered-out ones, and therefore no correction is necessary. This is not the case in our data, however, because the spectrum extraction regions of *Suzaku*/XIS and *NuSTAR*/FMP do not fully cover the dust-scattering halo. Hence, we have to estimate the fraction of the dust-scattering-halo photons contained in the spectrum extraction region (hereafter “scattering fraction”) and to correct for this effect in the spectral analysis.⁶ The situation becomes even more complex for a variable source because of the time delay between the direct and scattered-in components (see, e.g., Tiengo et al. 2010; Heinz et al. 2015, 2016).

In this paper, we follow the same procedures as those described in Hori et al. (2014). We estimate the scattering fraction to be 87% and 67% for the *Suzaku*/XIS spectra during the 2006 and 2015 outbursts, respectively, with the `FTOOL xissimarfgen` by assuming the image profile of the dust-scattering halo obtained by Smith et al. (2002).⁷ For the *NuSTAR*/FMP data, we approximately estimate it to be 66% by ignoring the point-spread function. Then, in the spectral fit, we utilize the `Dscat` model, which is a local model developed by

⁶ In reality, the effect of the point-spread function must also be taken into account for both direct and halo components.

⁷ We have confirmed that our results on the disk wind parameters do not change beyond the errors by adopting a different halo profile presented in Smith et al. (2016).

Table 1
Observation Log

OBSID	Suzaku Observation Date		XIS Option	Exposure (ks)			Flux (erg cm ⁻² s ⁻¹)	
	Start	End		Suzaku		NuSTAR	2–6 keV	12–30 keV
				XIS	PIN			
6	2006 Feb 8 15:09	Feb 9 3:20	1/4 window + 1s burst	11.1	20.5	...	3.4×10^{-9}	1.5×10^{-10}
5	2006 Feb 15 23:29	Feb 16 13:08	1/4 window + 1s burst	10.7	16.0	...	2.5×10^{-9}	1.2×10^{-10}
4	2006 Feb 28 23:18	Mar 1 16:43	1/4 window + 1s burst	10.7	17.9	...	2.4×10^{-9}	7.3×10^{-11}
3	2006 Mar 8 1:49	Mar 8 17:31	1/4 window	10.6	19.1	...	2.1×10^{-9}	5.0×10^{-11}
2	2006 Mar 15 5:26	Mar 15 17:51	1/4 window	23.2	17.7	...	1.9×10^{-9}	4.2×10^{-11}
1	2006 Mar 23 10:13	Mar 23 22:21	1/4 window	21.7	21.3	...	1.7×10^{-9}	3.7×10^{-11}
8	2015 Feb 20 5:41	Feb 21 9:52	1/4 window + 0.3s burst	5.3	...	16.5 ^a	4.4×10^{-9}	6.0×10^{-10}
7	2015 Feb 24 1:30	Feb 25 2:44	1/4 window + 0.3s burst	5.5	...	16.1 ^b	3.7×10^{-9}	1.4×10^{-10}
0	2015 Feb 27 2:28	Feb 28 3:42	1/4 window + 0.3s burst	5.1	3.7×10^{-9}	...
α	2012 Oct 2 0:24	Oct 2 20:38	1/4 window + 1s burst	2.9	39.5	...	6.6×10^{-9}	3.5×10^{-9}

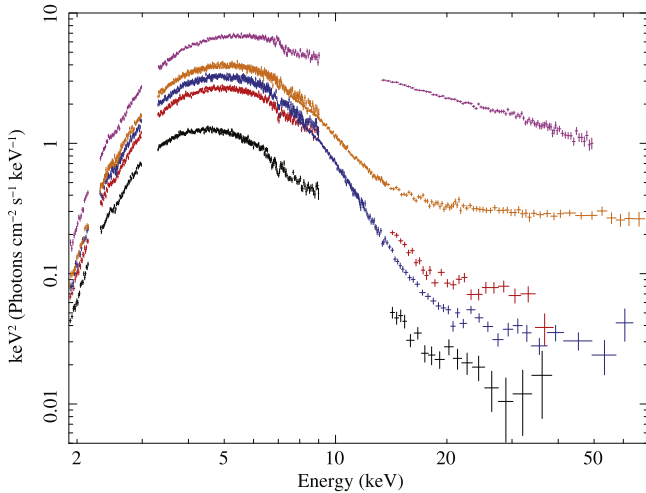
Notes.^a Observed between 2015 Feb 20 11:36 and Feb 20 23:31.^b Observed between 2015 Feb 24 10:46 and Feb 24 21:46.

Figure 3. The broadband spectra of 4U 1630–47 in the 2006 (black and red—OBS 1 and 6), 2015 (blue and orange—OBS 7 and 8), and 2012 (magenta—OBS α) outbursts. We plot the time-averaged *Suzaku*/XIS1 and *HXD* spectra in the range of 2–9 keV and 12–40 keV, respectively. The *HXD* was not operated during the 2015 outburst. The *NuSTAR*/FMPA spectra in the 2015 outburst are also plotted, which cover the 7.5–70 keV range. The *HXD* was operated in the 2012 outburst (magenta) when the source was in the VHS.

Ueda et al. (2010), to take into account the effects of dust-scattering. We check effects by time variability of 4U 1630–47 during the 2015 observations. The maximum time delay at the outer integration radius $1/2$ is estimated to be ~ 1 day by assuming that the scatterers are located at the half distance of 10 kpc (see, e.g., Heinz et al. 2015 for the calculation). The source shows a flux decay of $\sim 20\%$ around the *Suzaku* observations on this timescale (Figure 2(c)), which would lead to an enhancement of the scattering fraction by $< 4\%$ in OBS 8. We confirm that it does not affect our final results (Section 4). Hence, for simplicity, we ignore time variability in estimating the scattering fraction in the following analysis.

3.2. Continuum Modeling

Spectral analysis is performed separately to the data of OBS 1 through 8. We use the spectra of *Suzaku*/XIS, *Suzaku*/PIN, and

NuSTAR/FMPA in the energy range of 1.9–9.0 keV, 12–40 keV, and 6–80 keV, respectively. Conservatively, the XIS data above 9.0 keV are not utilized to minimize pileup effects, and those in the 2.1–2.3 keV and 3.0–3.4 keV are also excluded to avoid calibration uncertainties. The spectra of the two FI-XISs (XIS0 and 3) are summed together. Spectral fitting is performed by using *XSPEC* version 12.8.2.

We apply a conventional model consisting of a multi-color disk (MCD) component and a power law with a low energy cutoff (diskbb and simpl in *XSPEC* terminology, respectively). The simpl model has two free parameters, the photon index Γ and the fraction of the seed photons f_{PL} . To take into account adsorption by interstellar medium, we use the tbabs model with the Wilms et al. (2000) abundances and the Verner et al. (1996) cross section. To estimate the column density of iron ions in a simple manner, we utilize the “kabs” model (Ueda et al. 2004), an *XSPEC* local model calculating the Voigt profile from multiple fine-structure lines. The kabs model has three free parameters, the column density of each ion $N_{\text{ion}}^{\text{wind}}$, the velocity dispersion, which is fixed at 500 km s^{-1} in this analysis (Kubota et al. 2007), and the wind velocity v/c . The model is thus expressed as tbabs*Dscat*kabs*kabs*—simpl*diskbb in the *XSPEC* terminology, where the first and second kabs terms represent the absorption lines of H-like and He-like iron ions, respectively. We apply this model to all the XIS spectra in the 2006 and 2015 outbursts.

Table 2 summarizes the best-fit parameters and chi-squared value for each observation. Reasonably good fits are obtained with this model yielding the best-fit disk temperature of $T_{\text{disk}} \approx 1.2\text{--}1.4 \text{ keV}$ and photon index of $\Gamma \approx 2\text{--}3$. For OBS 0, Γ and f_{PL} are fixed to be 2.5 and 1.0%, respectively, because the spectrum only covered the energy range below 9 keV. During the 2006 outburst, the disk temperature and luminosity change together as expected in standard disk model to maintain a constant inner radius (Shakura & Sunyaev 1973). The inner disk radius (and column density) are slightly different in the 2015 outburst, most probably due to residual calibration uncertainties. The fraction f_{PL} is also almost constant from OBS 1–7 at around 1%, but then increases significantly in OBS 8.

Table 2
Best-fit Parameters for Spectral Modeling

Component	TBabs	diskbb		simpl			kabs		
Parameter	N_{H}^{a}	T_{in} (keV)	R_{in} (km)	Γ	f_{PL} (%)	$N_{\text{FeXXVI}}^{\text{b}}$	$N_{\text{FeXXV}}^{\text{b}}$	v_{wind} (km s $^{-1}$)	χ^2/dof
OBS 1	$7.85^{+0.03}_{-0.05}$	$1.16^{+0.01}_{-0.01}$	$27.2^{+0.5}_{-0.4}$	$3.20^{+0.42}_{-0.36}$	$1.1^{+0.7}_{-0.4}$	$1.59^{+0.39}_{-0.32}$	$0.58^{+0.18}_{-0.13}$	400^{+400}_{-400}	522/684
OBS 2	$7.85^{+0.05}_{-0.02}$	$1.19^{+0.01}_{-0.01}$	$27.2^{+0.4}_{-0.4}$	$2.03^{+0.37}_{-0.36}$	$0.3^{+0.2}_{-0.1}$	$1.21^{+0.28}_{-0.22}$	$0.37^{+0.10}_{-0.10}$	700^{+600}_{-600}	539/699
OBS 3	$7.99^{+0.06}_{-0.06}$	$1.20^{+0.01}_{-0.01}$	$28.3^{+0.5}_{-0.6}$	$2.38^{+0.30}_{-0.28}$	$0.5^{+0.3}_{-0.2}$	$1.18^{+0.41}_{-0.31}$	$0.32^{+0.14}_{-0.12}$	700^{+700}_{-600}	603/699
OBS 4	$8.04^{+0.05}_{-0.07}$	$1.22^{+0.01}_{-0.01}$	$28.5^{+0.4}_{-0.5}$	$2.42^{+0.22}_{-0.24}$	$0.8^{+0.3}_{-0.3}$	$1.11^{+0.39}_{-0.27}$	$0.25^{+0.11}_{-0.09}$	1400^{+600}_{-600}	557/696
OBS 5	$8.00^{+0.06}_{-0.05}$	$1.30^{+0.01}_{-0.01}$	$25.5^{+0.5}_{-0.4}$	$2.79^{+0.20}_{-0.19}$	$1.8^{+0.6}_{-0.4}$	$1.33^{+0.41}_{-0.31}$	$0.26^{+0.11}_{-0.09}$	1300^{+500}_{-500}	558/699
OBS 6	$8.06^{+0.05}_{-0.05}$	$1.34^{+0.01}_{-0.01}$	$27.0^{+0.3}_{-0.4}$	$2.27^{+0.14}_{-0.14}$	$0.9^{+0.3}_{-0.2}$	$1.04^{+0.26}_{-0.21}$	$0.08^{+0.06}_{-0.06}$	1300^{+600}_{-700}	576/713
OBS 7	$8.33^{+0.04}_{-0.02}$	$1.32^{+0.01}_{-0.01}$	$30.9^{+0.2}_{-0.3}$	$2.90^{+0.08}_{-0.08}$	$1.4^{+0.1}_{-0.2}$	$1.25^{+0.23}_{-0.19}$	$0.18^{+0.07}_{-0.05}$	1400^{+100}_{-100}	1422/1497
OBS 8	$8.40^{+0.04}_{-0.03}$	$1.35^{+0.01}_{-0.01}$	$32.2^{+0.2}_{-0.3}$	$2.24^{+0.02}_{-0.02}$	$3.3^{+0.1}_{-0.2}$	$0.30^{+0.06}_{-0.06}$	<0.02	1300^{+500}_{-400}	1454/1497
OBS 0	$8.46^{+0.04}_{-0.05}$	$1.32^{+0.01}_{-0.01}$	$31.7^{+0.3}_{-0.4}$	2.5(fixed)	1.0(fixed)	$0.90^{+0.21}_{-0.18}$	<0.04	2600^{+700}_{-700}	846/843

Notes.

^a Hydrogen column densities in the unit of 10^{22} cm $^{-2}$.

^b Ion column densities in the unit of 10^{18} cm $^{-2}$.

3.3. Long-term Variability of the Disk Wind

In this subsection, we focus on the iron-K absorption line features in OBS 1–8. No other line feature is significantly detected in the XIS spectra. Figure 4 shows the XIS unfolded spectra of OBS 1, 6, 7, and 8 in the 6–7.5 keV range together with the best-fit continuum model including the interstellar absorption and dust scattering. For comparison, we also plot the spectrum in the VHS (OBS α), which does not show any iron-K absorption line feature. Here we adopt the model D in Hori et al. (2014) for the continuum, which gives the best description of the *Suzaku* spectra. This model properly takes into account Comptonization of the inner disk emission with energetic coupling between the disk and corona, and the reflection of the Comptonized component from the accretion disk with general relativistic smearing effects. For further details, see Hori et al. (2014).

Figure 5 plots the column density of He-like and H-like irons against the 2–6 keV flux in the HSS during the 2006 (black) and 2015 outbursts (red). OBS 1 and OBS 6 are the faintest and brightest observations in the 2006 outburst, while OBS 7 and OBS 8 are the faintest and brightest observations in the 2015 outburst, respectively. The degree of ionization of the disk wind can be traced by the ratio of the column density in H-like to He-like iron. This gradually increases with 2–6 keV luminosity in the 2006 outburst, and then increases much more rapidly in the 2015 outburst, especially in the brightest observation, OBS 8. This result might be explained by photoionization of the disk wind because the observed X-ray spectrum shows significant hardening in the brightest observation owing to the increase of the hard tail component; we will quantitatively examine this possibility in the next section. We also note that the absorption lines in OBS 6 are weaker than those in OBS 7 as expected from the harder spectrum in OBS 6.

4. Discussions

Our *Suzaku* and *NuSTAR* observations of 4U 1630–47 during the 2015 outburst confirm the presence of absorption line features of highly ionized iron ions in the HSS spectra, which were reported by previous observations in the HSS during the 2006 outburst (Kubota et al. 2007). This strongly

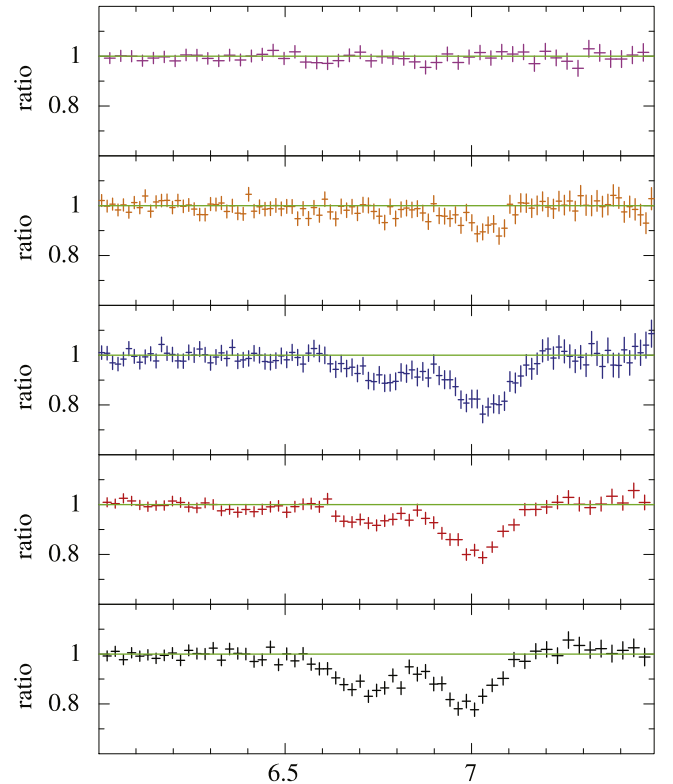


Figure 4. The unfolded spectra in the energy range of 6–7.5 keV during the 2006 (black and red), 2012 (magenta), and 2015 outbursts (blue and orange). Data of all XISs (XIS0, 1, and 3) are summed. The solid lines show the best-fit continuum model, excluding the *kabs* models (see the text). We also show the residuals between the data and best-fit models.

suggests that a highly (but not fully) ionized disk wind is always present in the HSS. These data enables us to investigate the evolution of the disk wind according to the change of luminosity and spectrum from a single source in detail.

4.1. A Simple Photoionized Simulation

We find that the ratio between the column densities of H-like and He-like iron ions increased at fluxes above $F_{2-6\text{keV}} \sim 3.5 \times 10^{-9}$ erg cm $^{-2}$ s $^{-1}$ where their spectra became harder with increasing contribution from the hard tail

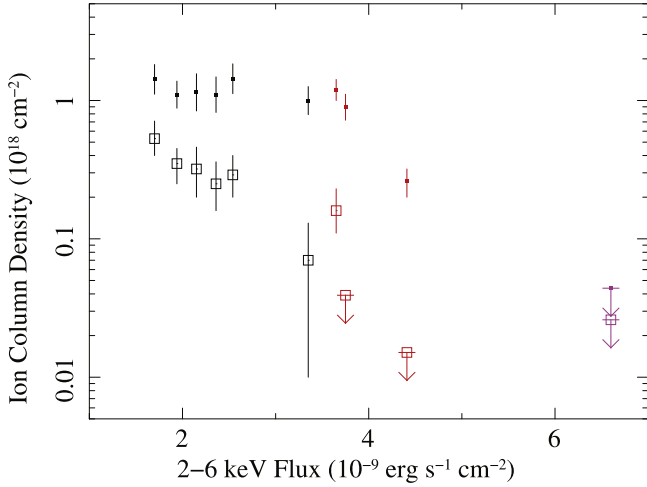


Figure 5. Correlation between the 2–6 keV flux and the column densities of iron ions obtained from the HSS spectra in the 2006 (black), 2012 (magenta), and 2015 (red) outbursts. The filled and squared dots represent the column densities of H-like and He-like iron ions, respectively.

(Figure 3). In order to examine whether an increase of photoionizing photons solely explains the observed increase of the ionization degree or not, we perform simulations of a photoionized gas, using XSTAR version 2.3. In XSTAR simulations, the ionization parameter of the absorber at the nearest point (i.e., the launching radius for a disk wind), ξ_0 , is defined as

$$\xi_0 = \frac{L_{\text{bol}}}{n_0 R_0^2}, \quad (2)$$

where L_{bol} is the luminosity in the 0.0136–13.6 keV band, R_0 is the distance of the absorber from the central source, and n_0 is the density. We use the observed continuum corrected for absorption and dust scattering in the 0.01–1000 keV range as the input of the source spectrum. To consider a self-similarly expanding wind with a constant velocity (Begelman et al. 1983), we assume a density (n) profile with respect to radius $R (> R_0)$ as $n = n_0 (R/R_0)^{-1.9}$, which gives an almost constant ionization parameter profile ($\xi = \xi_0 (R/R_0)^{-0.1}$).⁸ The turbulent velocity is set to be $V_{\text{urb}} = 500 \text{ km s}^{-1}$ in this simulation as a representative value, which has not been measured in this source (but not less than 100 km s^{-1} ; Kubota et al. 2007). To directly apply the simulation results to the *Suzaku*/XIS spectra, we make a grid *XSPEC* model of absorption by utilizing the XSTAR2XSPEC tool. Through the fitting, we are able to obtain the column density $N_{\text{H}}^{\text{wind}}$ and the ionization parameter ξ_0 .

We find that the higher ionization degree in OBS 8 than in the other HSS observations cannot be explained solely by the change of the source spectrum luminosity if we assume that the wind launching radius and density were the same as in the other epochs. This fact is found for the first time from 4U 1630–47, whereas similar results (i.e., that photoionization alone cannot explain changes of the ionization degree of a disk wind) were reported from other sources (Yamaoka et al. 2001 and

Neilsen & Homan 2012 for GRO J1655–40, Neilsen et al. 2012 for GRS 1915+105). In OBS 8, we are able to obtain only lower limits for ξ_0 and $N_{\text{H}}^{\text{wind}}$ because of the nondetection of He-like iron absorption line and of strong coupling between ξ_0 and $N_{\text{H}}^{\text{wind}}$. If we fix the column density at $N_{\text{H}}^{\text{wind}} = 2.3 \times 10^{23} \text{ cm}^{-2}$, which is obtained in OBS 7 showing the closest luminosity to that in OBS 8 (see Table 3), the ionization parameter in OBS 8 becomes $\xi_0 = 5.27_{-0.14}^{+0.19}$. This is significantly higher at a >90% confidence level than the value expected from the photoionization effect alone (i.e., the $\xi_0 = 4.74_{-0.12}^{+0.14}$, which is converted from the result of OBS 7 by replacing the luminosity with that of OBS 8). This result indicates that other physical parameters of the wind, such as wind launching radius R_0 and/or density at the launching radius n_0 , must have changed from OBS 7 to OBS 8.

4.2. Simulations of Photoionized Disk Wind

In the following, we show that these results can be explained by a theory of thermally driven winds. The Compton temperature T_{IC} and the wind escape velocity V_{wind} depend on the wind launching radius (or Compton radius, R_{IC}) as

$$kT_{\text{IC}} \propto \frac{GM_{\text{BH}}}{R_{\text{IC}}} \quad (3)$$

and

$$\frac{1}{2} V_{\text{wind}}^2 \propto \frac{GM_{\text{BH}}}{R_{\text{IC}}} \propto T_{\text{IC}}. \quad (4)$$

Here, k , G , and M_{BH} are the Boltzmann constant, the gravitational constant, and the mass of the BH, respectively. From numerical simulations, Woods et al. (1996) showed that the mass flux per unit area of an isothermal disk wind, \dot{m} , is given by

$$\dot{m} \sim 0.5 \left(\frac{kT_{\text{IC}}}{\mu} \right)^{-0.5} \frac{L}{4\pi R^2 c \Xi_{c,\text{crit}}}, \quad (5)$$

where μ , c , and $\Xi_{c,\text{crit}}$ are the mean mass per particle, the light speed, and the critical pressure ionization parameter determined by the spectrum, respectively. The mass-loss rate of the disk wind \dot{M} and the density at the base of the wind n_0 given as the following equations (Done et al. 2018)

$$\begin{aligned} \dot{M} &= 2 \int_{R_{\text{in}}}^{R_{\text{out}}} \dot{m} 2\pi R dR \\ &= \left(\frac{kT_{\text{IC}}}{\mu} \right)^{-0.5} \frac{L}{4\pi c \Xi_{c,\text{crit}}} \log \left(\frac{R_{\text{out}}}{R_{\text{in}}} \right) \\ &\propto L \times T_{\text{IC}}^{-0.5}, \end{aligned} \quad (6)$$

$$\begin{aligned} n_0 &= \frac{\dot{M}}{\Omega R_{\text{IC}}^2 V_{\text{wind}} m_p} \\ &\propto L \times T_{\text{IC}}. \end{aligned} \quad (7)$$

Here, R_{in} (R_{out}) is the inner (outer) disk radius, m_p is the proton mass, and Ω is the solid angle of the disk wind, which is assumed to be constant against the distance from the BH. The n_0 value in the OBS 1 is set to be $1.0 \times 10^{13} \text{ cm}^{-3}$, which yields the mean number density of $\bar{n} \sim 5 \times 10^{12} \text{ cm}^{-3}$ estimated by Kubota et al. (2007). In the following XSTAR

⁸ Here we adopt an index of -1.9 instead of -2.0 for the density profile because XSTAR calculations do not converge if we set $n \propto R^{-2}$ due to technical reasons. We have confirmed that our results are little affected by its choice within a range between -1.5 and -1.9 .

Table 3
 Fitting Results

Parameter	OBS 1	OBS 2	OBS 3	OBS 4	OBS 5	OBS 6	OBS 7	OBS 8
L_{bol} (10^{38} erg s^{-1}) ^a	1.20	1.34	1.48	1.61	1.63	2.13	2.61	3.14
T_{IC} (keV) ^b	0.70	1.37	0.92	0.99	0.95	1.38	0.83	3.25
n_0 (10^{13} cm^{-3}) ^c	1.0	2.1	1.6	1.9	1.8	3.5	2.6	12.0
$\log(\xi_0)$	$4.62^{+0.13}_{-0.11}$	$4.61^{+0.11}_{-0.11}$	$4.64^{+0.15}_{-0.14}$	$4.62^{+0.14}_{-0.14}$	$4.55^{+0.18}_{-0.10}$	$4.74^{+0.29}_{-0.17}$	$4.62^{+0.19}_{-0.15}$	>4.38
$N_{\text{H}}^{\text{wind}}$ (10^{23} cm^{-2})	$1.23^{+0.31}_{-0.24}$	$1.03^{+0.27}_{-0.23}$	$1.06^{+0.37}_{-0.30}$	$0.99^{+0.37}_{-0.29}$	$1.48^{+0.65}_{-0.37}$	$1.58^{+0.49}_{-0.47}$	$2.27^{+0.74}_{-0.60}$	>0.43
V_{wind} (km s^{-1})	500^{+400}_{-400}	800^{+500}_{-600}	800^{+700}_{-700}	1400^{+500}_{-600}	1400^{+500}_{-500}	1500^{+600}_{-600}	2200^{+500}_{-500}	2100^{+1200}_{-1100}

Notes.
^a Unabsorbed luminosities in the range of 0.0136–13.6 keV assuming isotropic emission.

^b Calculated by Equation (1) with the integration range of 0.01–1000 keV.

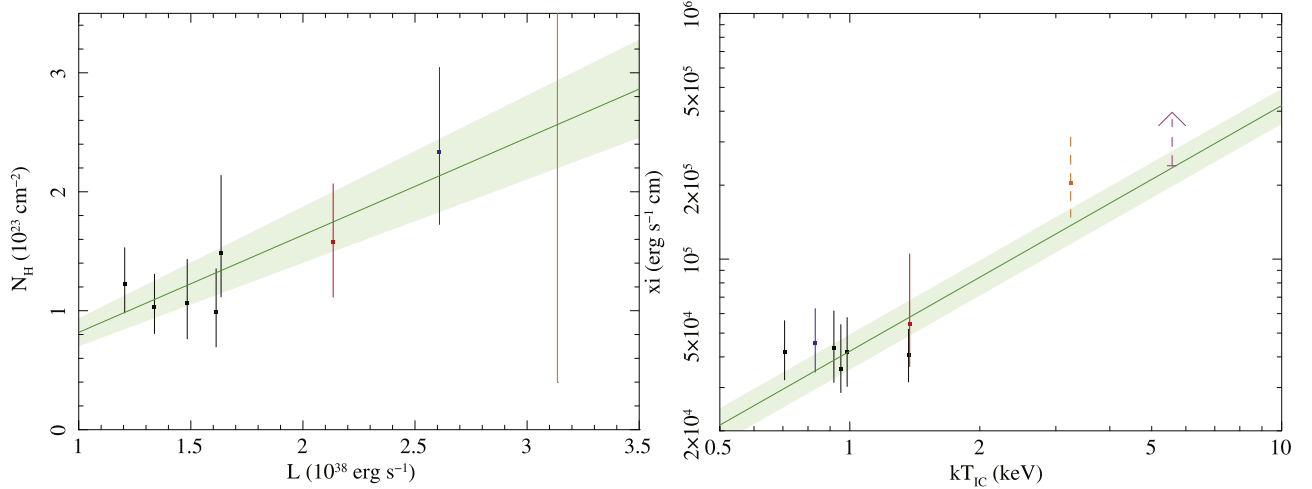
^c Calculated by Equation (7). n_0 in OBS 1 is set to be 1.0×10^{13} cm^{-3} .


Figure 6. (a) The L_{bol} dependence of the ion column density $N_{\text{H}}^{\text{wind}}$ and (b) the T_{IC} dependence of the ionization parameter ξ_0 . The black, red, and blue points represent the spectral fitting results (with 1σ errors) for OBS 1–5, 6, and 7, respectively. We only obtain the lower limit with OBS 8 (orange) due to the nondetection of the He-like iron absorption line. The green solid lines in (a) and (b) show the best-fit relation of Equations (8) and (9), respectively. The light green regions correspond to the 90% confidence interval. The orange dashed curve plots the best-fit ionization parameter by assuming a column density of $N_{\text{H}}^{\text{wind}} = 2.6 \times 10^{23}$ cm^{-2} . The magenta dashed arrows represent the lower limits for the VHS spectra in 2012 with an assumption of $N_{\text{H}}^{\text{wind}} = 4.4 \times 10^{23}$ cm^{-2} .

simulations, n_0 for each observation is calculated from Equation (7) (see Table 3). From these equations, we finally obtain the dependence of the column density $N_{\text{H}}^{\text{wind}}$ and the ionization parameter at the base of wind ξ_0 on luminosity and Compton temperature as

$$N_{\text{H}}^{\text{wind}} = \int_{R_{\text{IC}}}^{\infty} ndR \propto L \quad (8)$$

and

$$\xi_0 = \frac{L}{n_0 R_{\text{IC}}^2} \propto T_{\text{IC}}, \quad (9)$$

respectively.

The spectral fitting results (the best-fit values and 1σ errors of ξ_0 , $N_{\text{H}}^{\text{wind}}$, and V_{wind}) are summarized in Table 3 along with the luminosity L , Compton temperature kT_{IC} , and the density n_0 assumed in the XSTAR simulations. Figures 6(a) and (b) plots $N_{\text{H}}^{\text{wind}}$ against L , and ξ_0 against kT_{IC} , respectively. Only lower limits of $N_{\text{H}}^{\text{wind}}$ and ξ_0 are obtained in OBS 8 (orange arrows).

We have confirmed that correlation between $N_{\text{H}}^{\text{wind}}$ and L is significant at a 95% confidence level, by performing an F-test between the cases when we fit those data with a constant and with a linear function. The linear fit yields a slope of 0.67 ± 0.25 and a y-intercept of 0.23 ± 0.39 , which is consistent with zero. Accordingly, we fit the data again by assuming Equation (8) (i.e., proportional relation). The best-fit line with the 90% confidence interval is plotted in Figure 6(a), showing that all the data in OBS 1 through 8 are consistent with the theoretical relation. On the basis of our disk wind model, we are able to estimate the ionization parameter in OBS 8 to be $\log(\xi_0) = 5.31^{+0.18}_{-0.14}$ through the spectral fit, by adopting $N_{\text{H}}^{\text{wind}} = 2.56^{+0.37}_{-0.37} \times 10^{23}$ cm^{-2} predicted from Equation (8). This result is plotted in the orange dotted line in Figure 6(b). By including this data point, correlation between ξ_0 and T_{IC} is also confirmed at a 91% confidence level via an F-test. The best-fit relation of Equation (9) is plotted in Figure 6(b), with which all the data are consistent. We note that the possible increase of the scattering fraction in OBS 8 (discussed in Section 3.1) does not affect our final results. The maximum increase of the scattering fraction (4%) leads to an only $\sim 1\%$ luminosity decrease and a $\sim 2\%$ Compton temperature increase.

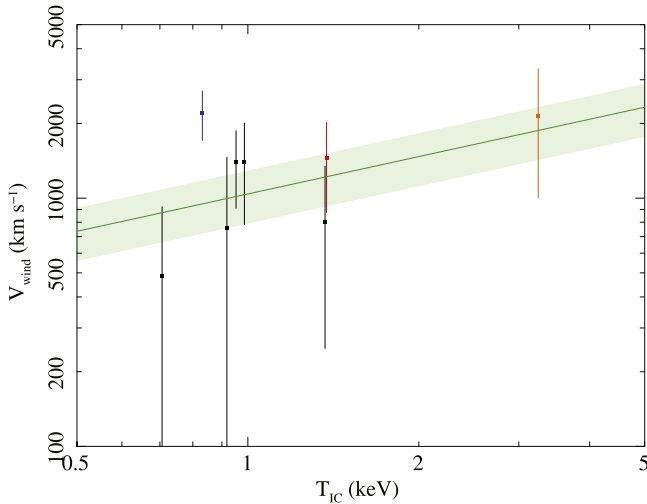


Figure 7. Relation between the best-fit wind velocity V_{wind} (with 1σ errors) and the Compton temperature T_{IC} . The black, red, blue, and orange points show that of OBS 1 to 5, 6, 7, and 8, respectively. The green line shows the best-fit relation of Equation (4) with the 90% confidence interval. We note that there are systematic errors of $\gtrsim 200 \text{ km s}^{-1}$ in V_{wind} due to calibration uncertainties.

The nondetection of the iron-K absorption lines in the VHS during the 2012 outburst does not contradict this theory. The column density and ionization parameter are predicted to be $N_{\text{H}}^{\text{wind}} = 4.39_{-0.63}^{+0.64} \times 10^{23} \text{ cm}^{-2}$ and $\log(\xi_0) = 5.37 \pm 0.07$ by using $L_{\text{bol}} = 5.36 \times 10^{38} \text{ erg s}^{-1}$ and $T_{\text{IC}} = 5.57 \text{ keV}$ with Equations (8) and (9). Analyzing the VHS spectra in the same way as for the HSS data, we obtain a lower limit of the ionization parameter of $\xi_0 > 5.38$ at a 99% confidence level. This is still consistent with the theoretical prediction (see Figure 6(b)). We do not rule out, however, the possibility that the geometrical configuration between the central source and outer disk might have changed in the VHS, leading to a more efficient ionization of the disk wind in the VHS than in the HSS. We note that runaway ionization of the wind via thermodynamical instability is unlikely to occur in the VHS (Chakravorty et al. 2013).

Figure 7 plots the relation between the wind velocity V_{wind} and the Compton temperature T_{IC} in the 2006 outburst. We find that the correlation is not statistically significant in our data, which are subject to large uncertainties. Nevertheless, the green line, representing the best-fit relation of $V_{\text{wind}} \propto T_{\text{IC}}^{0.5}$ (see Equation (4)), is consistent with the observed data except for OBS 7. We note that V_{wind} has a systematic error of $\sim 200 \text{ km s}^{-1}$ due to a possible energy-gain uncertainty of *Suzaku*/XIS, which became larger in the 2015 observations (OBS 7 and 8).⁹

From these results, we conclude that the evolution of the observed iron-K absorption line features in the spectra of 4U 1630–47 are consistent with a simple theory of thermally driven disk winds. We have shown that it is important to consider the dependence of the launching radius of a disk wind on the Compton temperature T_{IC} , which is determined by the shape of the continuum. Further observational studies with high-resolution spectroscopy that enable us to more accurately determine the outflow velocity would be useful to confirm our scenario.

⁹ https://heasarc.gsfc.nasa.gov/docs/astroe/prop_tools/suzaku_td/node10.html

Although the data and model agree fairly well, there are potential uncertainties in our calculation; here we assumed very simple velocity/density structures to predict the observable of thermally driven wind. Also we ignored the reduction of R_{IC} by radiation pressure, which becomes significant above $\sim 0.3L_{\text{Edd}}$ (Done et al. 2018). Hydrodynamic simulations and radiation transfer calculation based on their results would be required for more accurate discussion, which we left for future work.

5. Conclusions

We performed three observations of 4U 1630–47 with *Suzaku* during the 2015 outburst, simultaneously with *NuSTAR* in the first two epochs. For comparison, we also reanalyze the *Suzaku* data taken during the 2006 and 2012 outburst. The conclusions are summarized below.

1. The continuum in the HSS is well described by thermal disk emission and a weak power-law tail produced by Comptonization of the disk photons. The K absorption lines from highly ionized iron ions are detected in all observations in the HSS during the 2006 and 2015 outbursts.
2. We investigate the evolution of the disk wind parameters as a function of luminosity and spectrum. The degree of ionization dramatically increased at the brightest state during the 2015 outburst. The XSTAR simulations show that this change cannot be explained solely by photoionization effects if we assume constant launching radius and density of the wind.
3. We find that a simple theory of thermally driven winds can explain our observational results. We point out that the thermal disk winds respond to changes in the illuminating source flux and spectral shape. These parameters change the launch radius and density of the wind, which also affect its photoionization state.

We thank Fiona Harrison for approving our request for ToO observations of *NuSTAR* and the *Suzaku* and *NuSTAR* operation teams for scheduling the simultaneous observations. Part of this work was financially supported by the Grant-in-Aid for JSPS Fellows for young researchers (T.H.) and for Scientific Research 17K05384 (Y.U.). C.D. acknowledges STFC funding under grant ST/L00075X/1 and a JSPS long-term fellowship L16581. M.S. acknowledges support by the Special Postdoctoral Researchers Program at RIKEN.

ORCID iDs

Takafumi Hori  <https://orcid.org/0000-0001-8204-790X>
Yoshihiro Ueda  <https://orcid.org/0000-0001-7821-6715>

References

- Anders, E., & Grevesse, N. 1989, *GeCoA*, **53**, 197
 Begelman, M. C., McKee, C. F., & Shields, G. A. 1983, *ApJ*, **271**, 70
 Burrows, D. N., Hill, J. E., Nousek, J. A., et al. 2005, *SSRv*, **120**, 165
 Chakravorty, S., Lee, J. C., & Neilsen, J. 2013, *MNRAS*, **436**, 560
 Díaz Trigo, M., Migliari, S., Miller-Jones, J. C. A., & Guainazzi, M. 2014, *A&A*, **571**, A76
 Díaz Trigo, M., Sidoli, L., Boirin, L., & Parmar, A. N. 2012, *A&A*, **543**, A50
 Done, C., Gierliński, M., & Kubota, A. 2007, *A&Ar*, **15**, 1
 Done, C., Tomaru, R., & Takahashi, T. 2018, *MNRAS*, **473**, 838
 Harrison, F. A., Craig, W. W., Christensen, F. E., et al. 2013, *ApJ*, **770**, 103
 Heinz, S., Burton, M., Braiding, C., et al. 2015, *ApJ*, **806**, 265

- Heinz, S., Corrales, L., Smith, R., et al. 2016, *ApJ*, 825, 15
- Hori, T., Ueda, Y., Done, C., et al. 2016, *AN*, 337, 467
- Hori, T., Ueda, Y., Shidatsu, M., et al. 2014, *ApJ*, 790, 20
- Kallman, T. R., Bautista, M. A., Goriely, S., et al. 2009, *ApJ*, 701, 865
- King, A. L., Walton, D. J., Miller, J. M., et al. 2014, *ApJL*, 784, L2
- Kotani, T., Ebisawa, K., Dotani, T., et al. 2000, *ApJ*, 539, 413
- Kubota, A., Dotani, T., Cottam, J., et al. 2007, *PASJ*, 59, 185
- Levine, A. M., Bradt, H., Cui, W., et al. 1996, *ApJL*, 469, L33
- Matsuoka, M., Kawasaki, K., Ueno, S., et al. 2009, *PASJ*, 61, 999
- Miller, J. M., Raymond, J., Fabian, A., et al. 2006a, *Natur*, 441, 953
- Miller, J. M., Raymond, J., Homan, J., et al. 2006b, *ApJ*, 646, 394
- Miller, J. M., Raymond, J., Reynolds, C. S., et al. 2008, *ApJ*, 680, 1359
- Neilsen, J., & Homan, J. 2012, *ApJ*, 750, 27
- Neilsen, J., Petschek, A. J., & Lee, J. C. 2012, *MNRAS*, 421, 502
- Neilsen, J., Rahoui, F., Homan, J., & Buxton, M. 2016, *ApJ*, 822, 20
- Neilsen, J., Remillard, R. A., & Lee, J. C. 2011, *ApJ*, 737, 69
- Netzer, H. 2006, *ApJL*, 652, L117
- Penna, R. F., McKinney, J. C., Narayan, R., et al. 2010, *MNRAS*, 408, 752
- Ponti, G., Fender, R. P., Begelman, M. C., et al. 2012, *MNRAS*, 422, L11
- Shakura, N. I., & Sunyaev, R. A. 1973, *A&A*, 24, 337
- Shidatsu, M., Done, C., & Ueda, Y. 2016, *ApJ*, 823, 159
- Shidatsu, M., Ueda, Y., Nakahira, S., et al. 2013, *ApJ*, 779, 26
- Smith, R. K., Edgar, R. J., & Shafer, R. A. 2002, *ApJ*, 581, 562
- Smith, R. K., Valencic, L. A., & Corrales, L. 2016, *ApJ*, 818, 143
- Tiengo, A., Vianello, G., Esposito, P., et al. 2010, *ApJ*, 710, 227
- Ueda, Y., Honda, K., Takahashi, H., et al. 2010, *ApJ*, 713, 257
- Ueda, Y., Inoue, H., Tanaka, Y., et al. 1998, *ApJ*, 492, 782
- Ueda, Y., Murakami, H., Yamaoka, K., Dotani, T., & Ebisawa, K. 2004, *ApJ*, 609, 325
- Ueda, Y., Yamaoka, K., & Remillard, R. 2009, *ApJ*, 695, 888
- Uttley, P., & Klein-Wolt, M. 2015, *MNRAS*, 451, 475
- Verner, D. A., Ferland, G. J., Korista, K. T., & Yakovlev, D. G. 1996, *ApJ*, 465, 487
- Wilms, J., Allen, A., & McCray, R. 2000, *ApJ*, 542, 914
- Woods, D. T., Klein, R. I., Castor, J. I., McKee, C. F., & Bell, J. B. 1996, *ApJ*, 461, 767
- Yamaoka, K., Ueda, Y., Inoue, H., et al. 2001, *PASJ*, 53, 179
- Zdziarski, A. A., Poutanen, J., Paciesas, W. S., & Wen, L. 2002, *ApJ*, 578, 357